A Flexible AC Distribution System Device for a Microgrid

K. T. Tan, *Student Member, IEEE*, P. L. So, *Senior Member, IEEE*, Y. C. Chu, *Senior Member, IEEE*, and M. Z. Q. Chen, *Member, IEEE*

***Abstract*—This paper presents a flexible ac distribution system device for microgrid applications. The device aims to improve the power quality and reliability of the overall power distribution system that the microgrid is connected to. The control design employs a new model predictive control algorithm which allows faster computational time for large power systems by optimizing the steady-state and the transient control problems separately. Extended Kalman filters are also employed for frequency tracking and to extract the harmonic spectra of the grid voltage and the load currents in the microgrid. The design concept is verified through different test case scenarios to demonstrate the capability of the proposed device and the results obtained are discussed.**

***Index Terms*—Extended Kalman filter, microgrid, model predictive control, power quality.**

I. Introduction

THE concept of microgrid has offered consumers with increased reliability and reduction in total energy losses, and has become a promising alternative for traditional power distribution system [1], [2].

One area of study for the connection of a microgrid to the distribution grid is the impact of power quality (PQ) problems on the overall power system performance. These PQ problems include voltage and frequency deviations in the grid voltage and harmonics in the grid voltage and load currents. To overcome the aforementioned PQ problems, several power-conditioning equipments such as active filters [3], [4], uninterruptible power supplies [5], [6], dynamic voltage restorers [7], [8], and unified PQ conditioners [9] are usually employed by consumers to protect their loads and systems against PQ disturbances in the distribution network. However, these devices are usually installed at the consumer sides and the PQ problems that they are capable to handle are usually limited.

This paper proposes a flexible ac distribution system device for the microgrid that is realized using a combination of series and shunt voltage source inverters (VSIs). The proposed device is installed at the point of common coupling (PCC) of the distribution grid that the microgrid and other electrical loads are connected to. The proposed source for the dc-link voltage of the flexible ac distribution system device consists of a photovoltaic (PV) array and a battery to store the excess energy generated by the PV array and to provide power during sunless hours. The device is equipped with the capability to improve the PQ and reliability of the microgrid. Furthermore, during islanded operation of the microgrid, the device can provide real and reactive power to the microgrid. The proposed controller is based on a newly developed model predictive control (MPC) algorithm to track periodic reference signals for fast sampling linear time-invariant (LTI) systems that are subject to input constraints. This control methodology controls the input signals of the VSIs and decomposes the control problem into steady-state and transient subproblems which are optimized separately. In this way, the computational times can be greatly reduced.

In what follows, this paper provides a comprehensive solution for the operation of the flexible ac distribution system device for a microgrid based on a multi-input–multi-output (MIMO) state-space model. The device will accomplish the following tasks simultaneously:

1) compensating for harmonics in the grid voltage and load currents;
2) real and reactive power control for load sharing during peak periods and power factor correction at the grid side;
3) maintaining PQ despite slight voltage and frequency variations in the grid voltage; and
4) momentarily dispatching real and reactive power to the microgrid when it becomes islanded.

II. System Description

The configuration of the microgrid considered in this paper for implementation of the flexible ac distribution system device is shown in Fig. 1. The proposed microgrid consists of three radial feeders (1, 2 and 3) where feeders 1 and 3 are each connected to a distributed generation (DG) unit consisting of a microgenerator, a three-phase VSI, and a three-phase LC filter. Feeder 2, however, is connected to an electrical load. The load types in the microgrid will be discussed in Section VI.

The flexible ac distribution system device is operated in two modes: 1) PQ compensation and 2) emergency operation. During grid-connected operation, the microgrid is connected to the distribution grid at the PCC. In this mode, the two DG units are controlled to provide local power and voltage support for loads 1–3 and hence reduce the burden of generation and delivery of

Manuscript received September 3, 2012; revised March 14, 2013; accepted April 16, 2013. Date of publication May 20, 2013; date of current version August 16, 2013. This work was supported by the School of Electrical and Electronic Engineering, Nanyang Technological University, Singapore, and also by A*STAR under the Smart Grid Project (SERC Grant No. 112 120 2022). The work of M. Z. Q. Chen and Y. C. Chu was supported by HKU CRCG Fund 201111159110. The work of M. Z. Q. Chen was also supported by NNSFC 61004093. Paper no. TEC-00461-2012.

The authors are with Nanyang Technological University, Singapore 639798, and also with the University of Hong Kong, Hong Kong (e-mail: eplso@ntu.edu.sg).

Digital Object Identifier 10.1109/TEC.2013.2260162

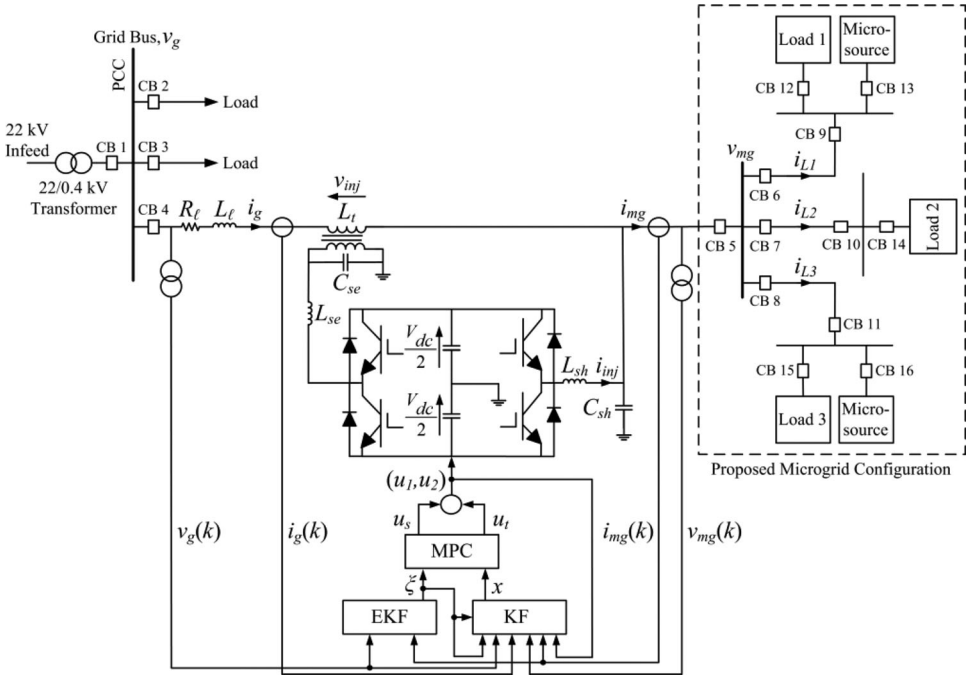

Fig. 1. Overall configuration of the proposed flexible ac distribution system device and the microgrid architecture with EKF denoting the extended Kalman filter and KF denoting the Kalman filter for the plant.

power directly from the utility grid. The flexible ac distribution system device functions to compensate for any harmonics in the currents drawn by the nonlinear loads in the microgrid so that the harmonics will not propagate to the rest of the electrical loads that are connected to the PCC. The device also functions to compensate for harmonics in the grid voltage that are caused by other nonlinear loads that are connected at the PCC. The energization of large loads and rapid changes in the load demand may also result in voltage and frequency variations in the grid voltage. Therefore, the device is also equipped with the capability to handle such voltage and frequency variations.

When a fault occurs on the upstream network of the grid, the CBs operate to disconnect the microgrid from the grid. The DG units are now the sole power sources left to regulate the loads. In the case when the generation capacity of the microgenerators is unable to meet the total load demand, the flexible ac distribution system device transits to operate in the emergency mode and functions to momentarily provide for the shortage in real and reactive power. In Fig. 2, the detailed configuration of the three-phase flexible ac distribution system device is shown.

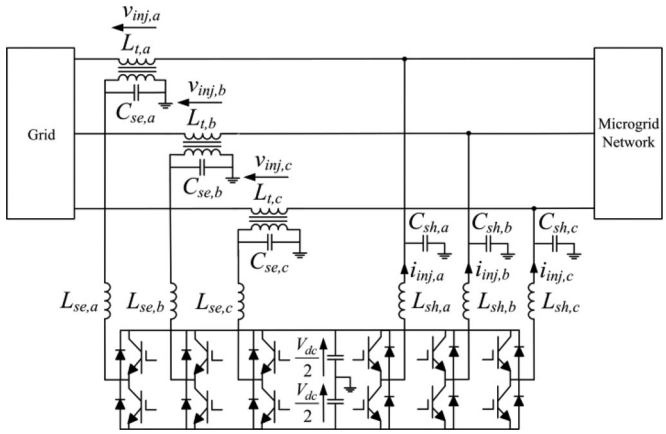

Fig. 2. Configuration of the three-phase flexible ac distribution system device.

III. Flexible AC Distribution System Device Model

The single-phase representation of the flexible ac distribution system device is shown in Fig. 3 [10]. The distribution grid voltage at the PCC and the total current drawn by the microgrid are modeled as v_g and $i_{\rm mg}$, respectively. With the proliferation of power electronics equipment being connected to the distribution grid and the microgrid, both v_g and $i_{\rm mg}$ could be distorted due to the presence of harmonic components. Therefore, v_g is modeled as a source consisting of its fundamental v_f and harmonic v_h that can be represented by

$$v_g = v_f + v_h = V_f \sin(\omega t) + \sum_{h=3,5,\ldots}^{N} V_h \sin(h\omega t - \theta_h) \quad (1)$$

where v_f is the fundamental component of v_g with its peak amplitude V_f and v_h is a combination of the harmonic components of v_g with its peak amplitude V_h and phase angle θ_h. To compensate for the harmonics in v_g, the series VSI injects a voltage $v_{\rm inj}$ that is given by

$$v_{\rm inj} = v_h - v_z - v_t \quad (2)$$

where v_z is the voltage drop across the line impedance of R_ℓ and L_ℓ, and v_t is the voltage drop across the equivalent leakage reactance L_t of the series-connected transformer. Similarly, $i_{\rm mg}$

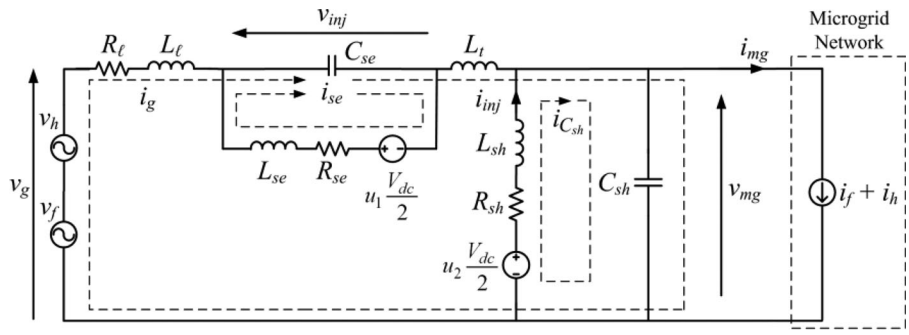

Fig. 3. Single-phase representation of the flexible ac distribution system device.

is also modeled as two components consisting of fundamental i_f and harmonic i_h with their peak amplitudes I_f and I_h, respectively and is represented by

$$\begin{aligned} i_{\rm mg} &= i_f + i_h = I_f \sin(\omega t - \varphi_f) + \sum_{h=3,5,\ldots}^{N} I_h \sin(h\omega t - \varphi_h) \\ &= I_f \sin\omega t \cos\varphi_f - I_f \cos\omega t \sin\varphi_f \\ &\quad + \sum_{h=3,5,\ldots}^{N} I_h \sin(h\omega t - \varphi_h) = i_{f,p} + i_{f,q} + i_h \end{aligned} \tag{3}$$

where φ_f and φ_h are the respective phase angles of the fundamental and harmonic components of $i_{\rm mg}$, and $i_{f,p}$ and $i_{f,q}$ are the instantaneous fundamental phase and quadrature components of $i_{\rm mg}$. To achieve unity power factor at the grid side, compensate for the harmonics in the microgrid current and achieve load sharing concurrently, the shunt VSI injects a current $i_{\rm inj}$ that is given by

$$i_{\rm inj} = (i_{f,p} - i_g) + i_{f,q} + i_h + i_{C_{\rm sh}} \tag{4}$$

where i_g is the grid current. The switched voltage across the series and shunt VSIs of the flexible ac distribution system device are represented by $u_1\ (V_{\rm dc}/2)$ and $u_2\ (V_{\rm dc}/2)$, respectively. To eliminate the high switching frequency components generated by the series and shunt VSIs, two second-order low-pass interfacing filters which are represented by $L_{\rm se}, C_{\rm se}, L_{\rm sh}$, and $C_{\rm sh}$ are incorporated. The losses of the series and shunt VSIs are modeled as $R_{\rm se}$ and $R_{\rm sh}$, respectively.

To derive a state-space model for the aforementioned system, Kirchhoff's voltage and current laws are applied to the three current loops as shown in Fig. 3.

The following equation is obtained from loop i_g:

$$v_g = i_g R_\ell + (L_\ell + L_t)\frac{di_g}{dt} + v_{\rm inj} + v_{\rm mg}. \tag{5}$$

The following equations are obtained from loop $i_{\rm se}$:

$$\frac{V_{\rm dc}}{2}u_1 = i_{\rm se}R_{\rm se} + L_{\rm se}\frac{di_{\rm se}}{dt} + v_{\rm inj} \tag{6}$$

$$v_{\rm inj} = \frac{1}{C_{\rm se}}\int (i_g + i_{\rm se})dt. \tag{7}$$

The following equations are obtained from loop i_{Csh}:

$$\frac{V_{\rm dc}}{2}u_2 = i_{\rm inj}R_{\rm sh} + L_{\rm sh}\frac{di_{\rm inj}}{dt} + v_{\rm mg} \tag{8}$$

$$v_{C\rm sh} = \frac{1}{C_{\rm sh}}\int i_{C\rm sh}dt \tag{9}$$

$$i_{\rm mg} = i_g + i_{\rm inj} - i_{C\rm sh} = i_{L1} + i_{L2} + i_{L3} + \cdots + i_{Lk} \tag{10}$$

where k is the number of feeders that are connected to the microgrid. By rearranging (5)–(10), the state-space representation of the system can be obtained as

$$\dot{x} = \bar{A}x + \bar{B}_1 w + \bar{B}_2 u \tag{11}$$

$$y = Cx + D_1 w + D_2 u \tag{12}$$

where

$$\bar{A} = \begin{bmatrix} -\dfrac{R_\ell}{(L_\ell + L_t)} & 0 & 0 & -\dfrac{1}{(L_\ell + L_t)} & -\dfrac{1}{(L_\ell + L_t)} \\ 0 & -\dfrac{R_{\rm se}}{L_{\rm se}} & 0 & -\dfrac{1}{L_{\rm se}} & 0 \\ 0 & 0 & -\dfrac{R_{\rm sh}}{L_{\rm sh}} & 0 & -\dfrac{1}{L_{\rm sh}} \\ \dfrac{1}{C_{\rm se}} & \dfrac{1}{C_{\rm se}} & 0 & 0 & 0 \\ \dfrac{1}{C_{\rm sh}} & 0 & \dfrac{1}{C_{\rm sh}} & 0 & 0 \end{bmatrix}$$

$$\bar{B}_1 = \begin{bmatrix} \dfrac{1}{L_\ell} & 0 \\ 0 & 0 \\ 0 & 0 \\ 0 & 0 \\ 0 & -\dfrac{1}{C_{\rm sh}} \end{bmatrix} \quad \bar{B}_2 = \begin{bmatrix} 0 & 0 \\ \dfrac{V_{\rm dc}}{2L_{\rm se}} & 0 \\ 0 & \dfrac{V_{\rm dc}}{2L_{\rm sh}} \\ 0 & 0 \\ 0 & 0 \end{bmatrix}$$

$$C = \begin{bmatrix} 0 & 0 & 0 & 0 & 1 \\ 1 & 0 & 0 & 0 & 0 \end{bmatrix} \quad D_1 = \begin{bmatrix} 0 & 0 \\ 0 & 0 \end{bmatrix} \quad D_2 = \begin{bmatrix} 0 & 0 \\ 0 & 0 \end{bmatrix}$$

$x = [\, i_g \quad i_{\rm se} \quad i_{\rm inj} \quad v_{\rm inj} \quad v_{C\rm sh}\,]^T$ is the state vector; $u = [\, u_1 \quad u_2\,]^T$ is the control input, with $-1 \le u_k \le 1, k = 1, 2$; $w = [\, v_g \quad i_{\rm mg}\,]^T$ is the periodic exogenous signal; and $y = [\, v_{\rm mg} \quad i_g\,]^T$ is the output, which will be regulated to track the desired sinusoidal reference waveforms.

IV. Control Design

With the mathematical model presented in Section III, this paper proposes a new MPC algorithm for the flexible ac distribution system device. The proposed algorithm is an extension of a recently developed MPC algorithm in [11], which is specifically designed for fast-sampling systems like the proposed flexible ac distribution system device to track periodic signals. This algorithm decomposes the MPC optimization into two subproblems: a steady-state subproblem and a transient subproblem, which are solved in parallel in different time scales, thus reducing the computational burdens. However, the MPC algorithm in [11] assumes that the periodic signals have a fixed and known frequency. In this paper, the algorithm is extended to allow an unknown frequency so that it will also be suitable for tracking frequency variations.

It is known that any periodic signal with a finite number of harmonics can be written as the output of an autonomous finite-dimensional LTI state-space model. For example, if the periodic signal has a fundamental frequency ω and consists of only odd harmonics, the A-matrix of the corresponding state-space model can take a block diagonal form with the blocks given by $\left[\begin{smallmatrix} 0 & h\omega \\ -h\omega & 0 \end{smallmatrix}\right]$ where $h = 1, 3, 5, \ldots$, and the C-matrix $[\,1 \quad 0 \quad 1 \quad 0 \quad \ldots \quad 1 \quad 0\,]$. Furthermore, the initial state of this autonomous model determines the magnitude and phase angle of this periodic signal. In this way, the exogenous signal $w = [\,v_g \quad i_{\mathrm{mg}}\,]$ in (11) and (12) can be modeled by

$$\dot{\xi} = \bar{A}_\xi\,(\omega_g, \omega_{\mathrm{mg}})\,\xi \tag{13}$$

$$w = C_w \xi \tag{14}$$

where the matrix $\bar{A}_\xi$ is parameterized by the distribution grid fundamental frequency ω_g and the microgrid fundamental frequency ω_{mg}, both of which should ideally be 50 Hz. On the other hand, the desired references that v_{mg} and i_g are to track can be represented by

$$d = [\,dv_{\mathrm{mg}} \quad di_g\,]^T = C_d \xi \tag{15}$$

To accomplish the goals specified in Section I, dv_{mg} should be regulated to a pure sine wave with a fixed magnitude. For any sag or swell that might occur in v_g, the control system is designed to maintain the magnitude of v_{mg} even when the sag or swell occurs. To achieve this, dv_{mg} is decoupled from v_g after an initialization period so that v_{mg} will not be affected. The reference di_g is calculated from the amount of real and reactive power that is drawn from the distribution grid.

The state-space model (13)–(15) is called an exogenous system. In this paper, only odd harmonics up to the 29th order are considered, but the methodology can be easily extended to include even harmonics. The exogenous state ξ, which essentially represents the sets of Fourier coefficients of w and d, can be identified automatically using a Kalman-based linear observer from the signal w being measured and the reference d being specified, provided that the fundamental frequencies ω_g and ω_{mg} are both fixed and known. In our consideration, however, we assume that ω_{mg} is always desired to be 50 Hz whereas the distribution grid frequency ω_g may be subjected to slight but unknown variations, which needs to be estimated from the measurement of v_g. To achieve this, an augmented model of (13)–(15) in its discrete-time form is employed

$$\xi^+ = A_\xi(\omega_g, \omega_{\mathrm{mg}})\xi = e^{\bar{A}_\xi(\omega_g, \omega_{\mathrm{mg}})T_s}\xi \tag{16}$$

$$\omega_g^+ = \omega_g \tag{17}$$

$$w = C_w \xi \tag{18}$$

$$d = C_d \xi \tag{19}$$

where the superscript $+$ represents the time-shift and T_s is the sampling interval. This formulation treats the unknown parameter ω_g as a fixed but unknown state component that is required to be estimated too. As the augmented model (16)–(19) is now nonlinear, a linear observer is no longer appropriate and we propose to use an extended Kalman filter (EKF) to estimate ξ and identify ω_g simultaneously. More information along this line can be found in [12]. Note that the working principle of the EKF is based on linearization, which is only local. Fortunately, ω_g is known to be close to 50 Hz even though it may vary.

To apply the MPC algorithm, the state-space model (11) and (12) are discretized with a sampling interval of $T_s = 0.2$ ms, which is considered pretty fast in conventional MPC applications but necessary in our problem for the high order of harmonics being tackled. According to [13], sampling in the range of tens of kHz is possible with the state-of-the-art code generation techniques. Let the discrete-time version of (11) and (12) be written as

$$x^+ = Ax + B_1 w + B_2 u \tag{20}$$

$$y = Cx + D_1 w + D_2 u. \tag{21}$$

Following the argument in [11], we decompose the control u into a steady-state control u_s and a transient control u_t:

$$u = u_s + u_t \tag{22}$$

such that $u \to u_s$ and $u_t \to 0$ as $t \to \infty$. Both u_s and u_t will employ an MPC strategy, but the former will adopt a dynamic MPC policy whereas the latter will adopt a more conventional finite-horizon approach. The formulations of these two control designs are discussed in the following sections.

A. Steady-State Subproblem

Let $x \to x_s$ and $y \to y_s$ as $t \to \infty$ and $u \to u_s$. Then, according to (20) and (21), u_s, x_s, and y_s should satisfy

$$x_s^+ = Ax_s + B_1 w + B_2 u_s \tag{23}$$

$$y_s = Cx_s + D_1 w + D_2 u_s \tag{24}$$

subject to the constraint

$$|u_s| \le 1. \tag{25}$$

We consider the steady-state control u_s being generated from a dynamic MPC policy

$$\hat{\xi}^+ = A_{\hat{\xi}}(\omega_g, \omega_{\mathrm{mg}})\hat{\xi} \tag{26}$$

$$u_s = C_{\hat{\xi}}(\omega_g, \omega_{\mathrm{mg}})\hat{\xi} \tag{27}$$

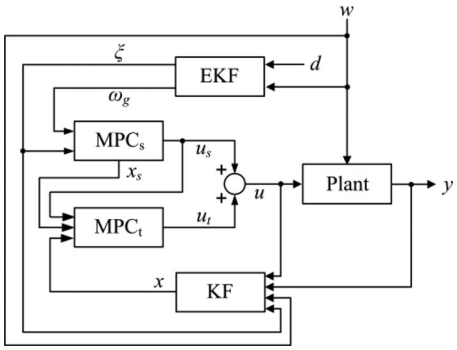

Fig. 4. Overall MPC controller for the flexible ac distribution system device.

where the matrices $A_{\hat{\xi}}$ and $C_{\hat{\xi}}$ are designed offline but the states $\hat{\xi}$ will be optimized online to minimize a quadratic penalty on the tracking error $e_s = y_s - d$, which is a linear function of the exogenous state ξ and the controller state $\hat{\xi}$, in a receding horizon fashion.

Then, with the estimates of ξ and ω_g provided by the EKF online, we can solve the following optimization problem:

$$\min_{\hat{\xi}(k)} \sum_i e_s\,(k+i)^T\, Q e_s(k+i) \text{ subject to } |u_s\,(k+i)| \le 1 \tag{28}$$

for some given positive definite matrix Q, to obtain the optimizer $\hat{\xi}(k)$ and accordingly $u_s\,(k)$, where the sum in (28) is done over a "nominal" period of 0.02 s. Note that the controller dynamics $A_{\hat{\xi}}$ and $C_{\hat{\xi}}$ depend on ω_g which has to be estimated online. To reduce the online computational burdens, we may precompute $A_{\hat{\xi}}$ and $C_{\hat{\xi}}$ for different values of ω_g and store them in the memory in advance. This is feasible because although ω_g is uncertain, it is supposed to vary only in a small range around 50 Hz.

B. Transient Subproblem

The transient signals are defined by $u_t = u - u_s, x_t = x - x_s$, and $y_t = y - y_s$. Then, according to (20) and (21), and (23) and (24), u_t, x_t, and y_t should satisfy

$$x_t^+ = Ax_t + B_2 u_t \tag{29}$$

$$y_t = Cx_t + D_2 u_t. \tag{30}$$

In this transient subproblem, the objective is to make $y_t \to 0$ as fast as possible, subject to the constraint

$$|u_s + u_t| \le 1. \tag{31}$$

In this paper, a more conventional approach of MPC that employs a finite horizon with a terminal cost is adopted. The information required by the MPC includes u_s and x_s, which will be provided by the solution of the steady-state subproblem, and the plant state x, which can be estimated using a plant Kalman filter. The overall configuration of the proposed control strategy combining the steady-state control u_s and the transient control u_t is shown in Fig. 4.

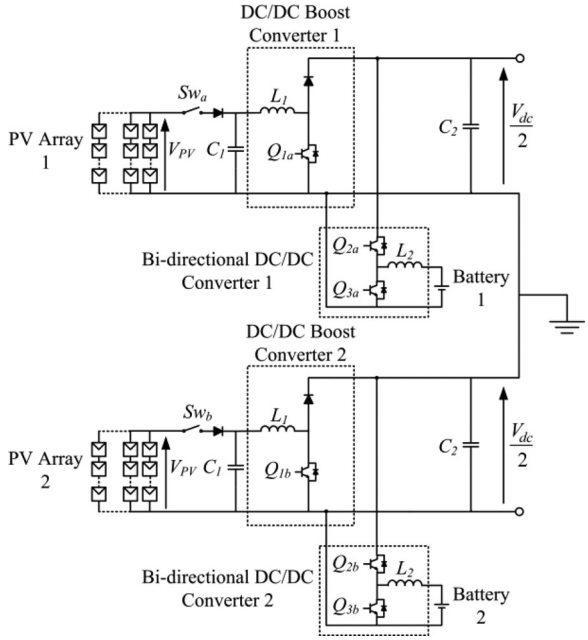

Fig. 5. Proposed PV/battery system for the device.

V. Proposed Hybrid Source for DC-Link Voltage

The proposed source for the dc-link voltage of the flexible ac distribution system device consists of a PV array and a battery as shown in Fig. 5. The PV array and the battery are connected to the VSI of the device through a boost converter and a buck–boost converter, respectively, to facilitate charging and discharging operations for the battery and to regulate the dc-link voltage at the desired level.

To maintain the dc-link at the reference voltage $V_{\rm dc}^*/2$, a dual loop control scheme in [14], which consists of an outer voltage loop and an inner current loop for the bidirectional converter, is implemented to compensate for the variation in the output voltage $V_{\rm dc}/2$ of the dc/dc boost converter. In this section, the operation of the PV/battery system is briefly explained.

When there is ample sunlight, the PV array is controlled by the dc/dc boost converter to operate in the MPPT mode to deliver its maximum dc power P_{pv} at $V_{\rm dc}/2$, which induces a voltage error $(V_{\rm dc}^*/2 - V_{\rm dc}/2)$ at the dc-link. The error is passed to a PI controller, which produces a reference battery current i_b^* for the inner current loop to operate the battery in either the charging mode for a positive error or discharging mode for a negative error. When the battery is in the charging mode, the bidirectional converter operates as a buck converter by turning switch Q_{3a} OFF and applying the control signal from the controller to switch Q_{2a} ON as shown in Fig. 6. Conversely, when the battery is in the discharging mode, the bidirectional converter operates as a boost converter by turning switch Q_{2a} OFF and applying the control signal from the controller to switch Q_{3a} ON as shown in Fig. 7.

Figs. 6 and 7 illustrate the charging and discharging operations of Battery 1, so as to maintain the upper dc-link voltage at a desired value. The same charging and discharging operations are applied to Battery 2 such that the dc-link voltages for

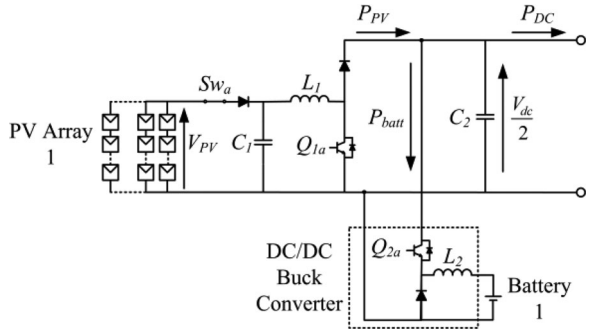

Fig. 6. Equivalent circuit during charging operation.

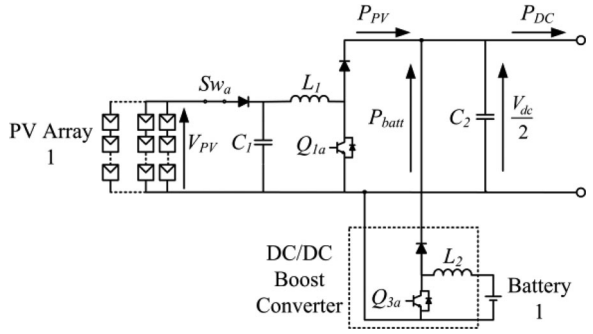

Fig. 7. Equivalent circuit during discharging operation.

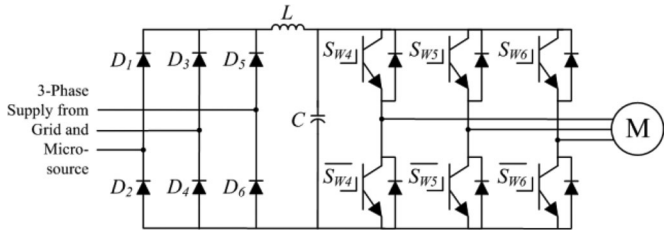

Fig. 8. Configuration of a 15kVA three-phase ASD.

both the upper and lower dc-link capacitors are maintained at $V_{\rm dc}^*/2$. When the PV array is subject to prolonged period of sunless hours and the state-of-charge of the battery falls below a preset limit, a self-charging technique from the grid can be incorporated into the design of the device. The design of this self-charging technique is detailed in [4].

VI. Numerical Simulation Analysis

The proposed device is tested under different case scenarios using MATLAB/Simulink to evaluate its capability to improve the PQ and reliability of the distribution network that the microgrid is connected to. Different types of loads consisting of linear and nonlinear loads for the microgrid are considered in these test cases. For load 1, a 15kVA three-phase PWM adjustable speed drive (ASD) with its configuration as shown in Fig. 8 is used. Load 2 is made up of a three-phase linear load and load 3 consists of a three-phase dimmer load which is nonlinear in nature. The per-phase currents i_{L1}, i_{L2}, and i_{L3} drawn by the feeders 1, 2, and 3 are shown in Fig. 9. The system parameters are given in Table I. The impedance of the distribution line is

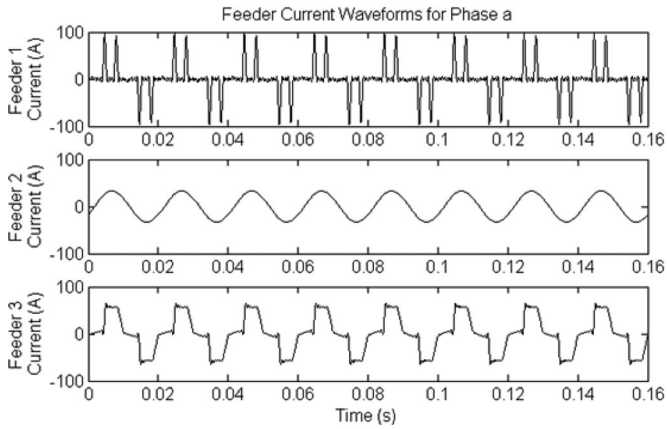

Fig. 9. Per-phase currents drawn by feeders 1, 2, and 3.

TABLE I
Parameters of the Proposed System

Parameter	Value
Distribution grid voltage	v_g = 230V (phase)
DC link voltage	V_{dc} = 800V
Distribution line impedance	R_ℓ = 7.5mΩ, L_ℓ = 25.7μH
Series inductance	L_{se} = 5mH
Series capacitance	C_{se} = 10μF
Series loss resistance	R_{se} = 0.01Ω
Shunt inductance	L_{sh} = 1.2mH
Shunt capacitance	C_{sh} = 20μF
Shunt loss resistance	R_{sh} = 0.01Ω
Transformer leakage inductance	L_t = 50μH

obtained according to [15]. The DG inverter loss resistance has been coarsely estimated because it is not precisely known in practice.

A. Test Case 1: Harmonic Compensation and Power Factor Correction During Steady-State Operation With Load Sharing

In the first test case, the capability of the flexible ac distribution system device to perform harmonic compensation for grid voltage v_g (due to nonlinear loads connected to the grid bus) and microgrid current $i_{\rm mg}$ (due to the nonlinear loads connected to the microgrid) as well as power factor correction during steady-state operation is demonstrated. The device is also controlled to deliver real power to the microgrid during peak periods when the cost of generation from the grid is high. By doing so, the power required from the grid is reduced and peak shaving is achieved. As such, the device is tasked to deliver 20% and 40% of the real power to the microgrid for $0 \leq t < 0.16$ s and $0.16 \leq t < 0.32$ s, respectively, while the grid delivers 80% and 60% of the real power to the microgrid.

The voltage and current waveforms under this test case are shown in Figs. 10 and 11, respectively. During steady-state operation, the total harmonic distortion (THD) values of v_g and $i_{\rm mg}$ are 18.39% and 42.1%, respectively. With the device injecting the voltage and current harmonics as shown in the middle

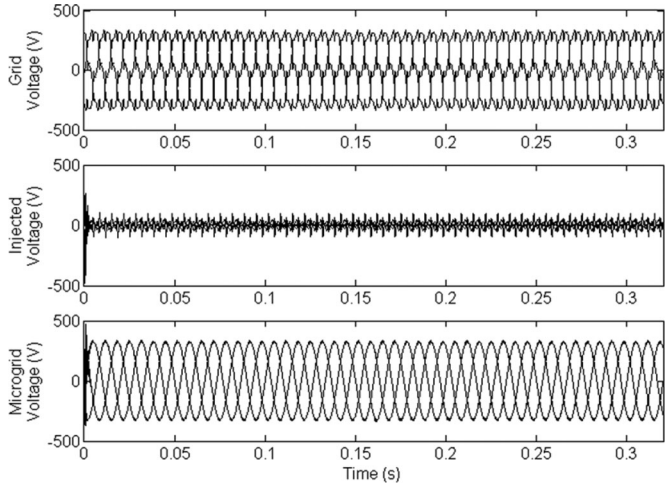

Fig. 10. (Top) Grid voltage v_g, (middle) injected voltage $v_{\rm inj}$ and (bottom) microgrid voltage $v_{\rm mg}$.

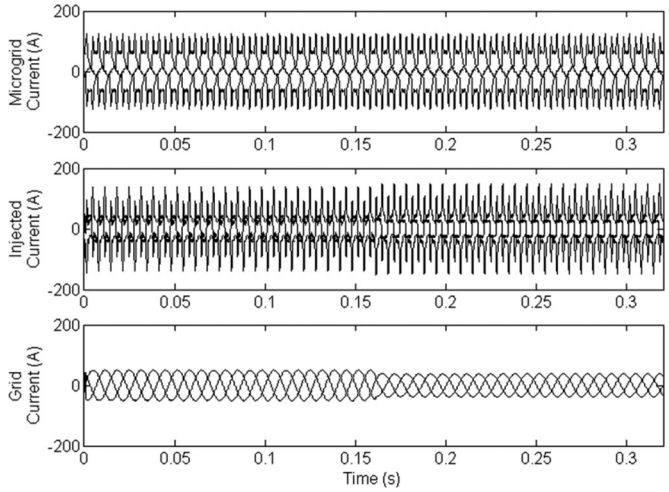

Fig. 11. (Top) Microgrid current $i_{\rm mg}$, (middle) injected current $i_{\rm inj}$, and (bottom) grid current i_g.

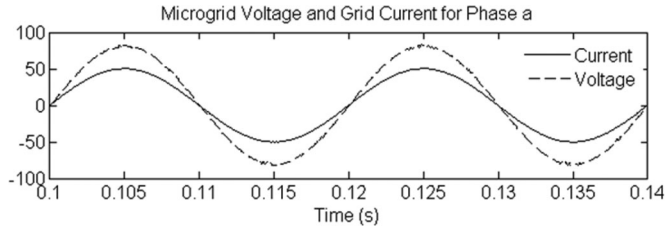

Fig. 12. Waveforms of microgrid voltage $v_{\rm mg}$ and grid current i_g.

waveforms of Figs. 10 and 11, the THD values of $v_{\rm mg}$ and i_g are improved to about 1.5% and 0.4%, respectively as shown in the bottom waveforms of Figs. 10 and 11. To achieve power factor correction at the grid side, the device is also controlled to provide the reactive component $i_{f,q}$ of the microgrid current $i_{\rm mg}$ as given in (4). A close-up waveform for $v_{\rm mg}$ (the voltage has been scaled down by a factor of 0.25 for comparison) and i_g for $0.1 \leq t < 0.14$ s is shown in Fig. 12. It can be observed

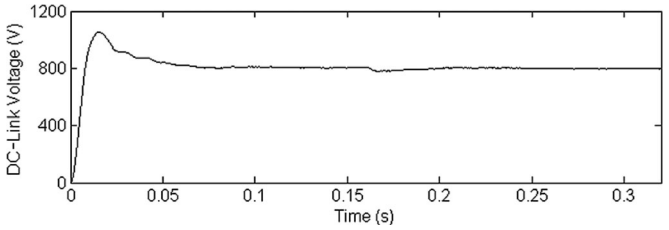

Fig. 13. DC-link voltage of the flexible ac distribution system device.

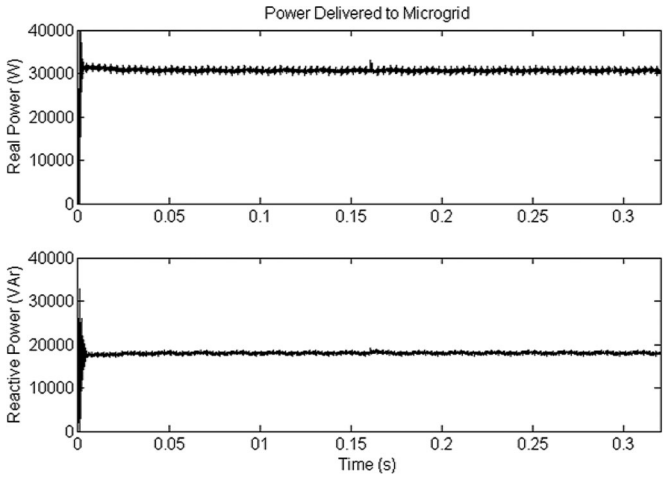

Fig. 14. (Top) Real and (bottom) reactive power delivered to the microgrid.

that the waveform of i_g is in phase with that of $v_{\rm mg}$ to achieve power factor correction.

From Fig. 13, it can be seen that the dc-link voltage V_{dc} takes a period of about three cycles to settle and stabilize at the reference value of 800 V, and the voltage ripple is maintained well within an acceptable range of about $\pm$ 1.25%. At $t = 0.16$ s, the increase in the generation demand from the device causes a small dip in the dc-link voltage which is quickly restored back to the preset value.

The total real and reactive power delivered to the microgrid is about 32 kW and 19kVAr as shown in Fig 14. The real power dispatched by the device is 6.4 kW (20% of the real power delivered to the microgrid) for $0 \leq t < 0.16$ s and 12.8 kW (40% of the real power delivered to the microgrid) for $0.16 \leq t < 0.32$ s as shown in Fig. 15, which illustrates the capability of the device to dispatch the required power. The device also delivers all the reactive power of 19kVAr required by the microgrid to achieve unity power factor at the grid side. As shown in Fig. 16, the real power delivered by the grid for $0 \leq t < 0.16$ and $0.16 \leq t < 0.32$ s are 80% (25.6 kW) and 60% (19.2 kW) of the total real power delivered to the microgrid and the reactive power supplied by the grid is zero resulting in unity power factor at the grid side.

B. Test Case 2: Sags and Swells in the Grid Voltage

In the second test case, the flexible ac distribution system device is controlled to cope with sags and swells in v_g. In this test case, a 30% sag for $0.12 \leq t < 0.24$ s and a 30% swell for $0.36 \leq t < 0.48$ s in v_g are simulated while the real and reactive

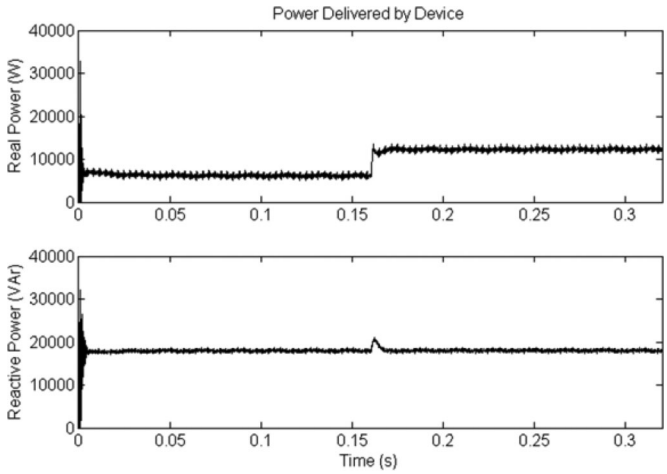

Fig. 15. (Top) Real and (bottom) reactive power delivered by the device.

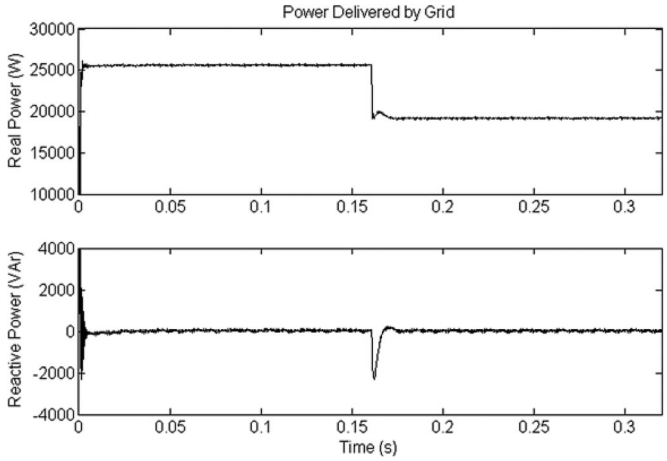

Fig. 16. (Top) Real and (bottom) reactive power delivered by the grid.

power required by the microgrid is kept constant throughout the entire interval. The voltage waveform for $0 \leq t < 0.48$ s is shown in Fig. 17. It can be observed that v_{mg} can still be regulated to the desired waveform even though the sag and swell cause a transient in v_{mg} which lasts for about three cycles. This can be achieved because dv_{mg} has been decoupled from v_g after the initialization period as discussed in Section IV.

C. Test Case 3: Frequency Variations in the Grid Voltage

In the third test case, the ability to handle slight frequency variations in v_g is demonstrated and two operating scenarios are presented. The voltage waveforms for $0 \leq t < 0.32$ s are shown in Fig. 18. In both test scenarios, the simulation begins with v_g operating at the nominal frequency of 50 Hz for $0 \leq t < 0.16$ s. The frequency of v_g then decreases to 49 Hz in the first test scenario as shown in Fig. 18 (top) and increases to 51 Hz in the second test scenario as shown in Fig. 18 (middle) for $0.16 \leq t < 0.32$ s. The real and reactive power required by the microgrid in both test scenarios remain constant.

It should be noted that in both test scenarios, the flexible ac distribution system device functions to maintain v_{mg} at 50 Hz and at the same time ensures that the frequency variations in

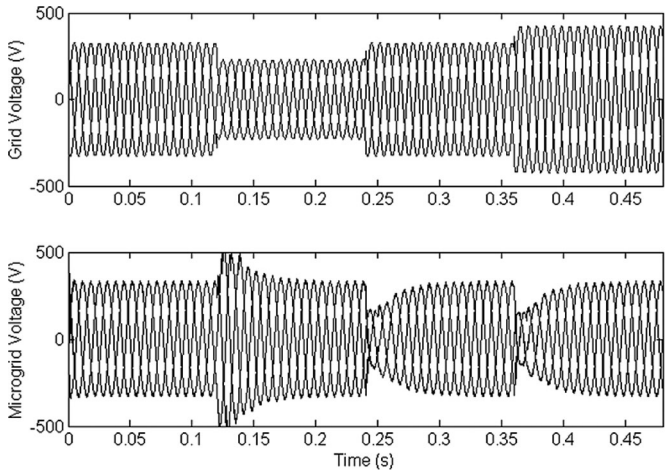

Fig. 17. (Top) Grid voltage v_g and (bottom) microgrid voltage v_{mg} during grid voltage sag and swell.

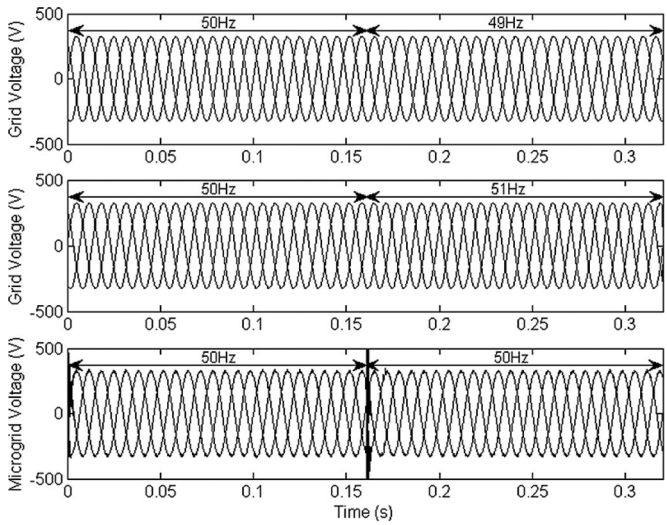

Fig. 18. Grid voltage v_g when frequency decreases to (top) 49 Hz and increases to (middle) 51 Hz and (bottom) microgrid voltage v_{mg}.

v_g do not cause any phase shift in v_{mg}. It is also observed from Fig. 18 (bottom) that the frequency variations in v_g under both test scenarios only cause a momentary disturbance to v_{mg} which lasts for about half a cycle and v_{mg} is then regulated to its nominal operating frequency of 50 Hz. This is achieved as the effect of slight frequency variations has been included in the augmented exogenous model of (16)–(19) and an EKF has been implemented to track for any frequency variations in v_g.

D. Test Case 4: Islanded Operation (Emergency Mode)

In the fourth test case, the flexible ac distribution system device is employed to momentarily provide real and reactive power to the microgrid when it becomes islanded. The real and reactive power waveforms delivered by the grid and device are shown in Figs. 19 and 20, respectively. The simulation begins with the microgrid operating connected to the grid for $0 \leq t < 0.16$ s. The grid is supplying the real power demand of 32 kW to the microgrid as shown in Fig. 19. As shown in

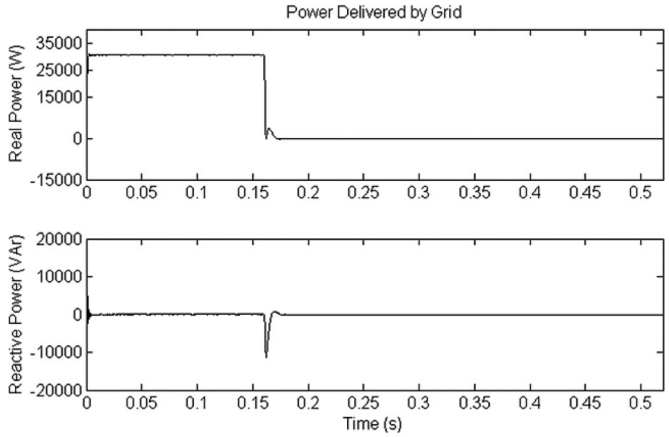

Fig. 19. (Top) Real and (bottom) reactive power delivered by the grid.

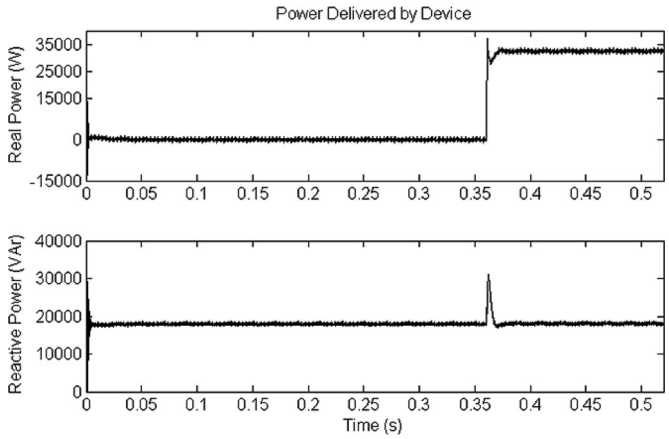

Fig. 20. (Top) Real and (bottom) reactive (bottom) power delivered by the device.

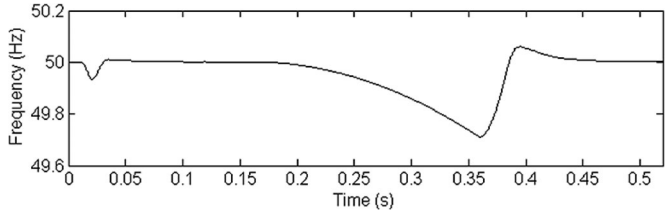

Fig. 21. System frequency response when the microgrid transits from grid-connected to islanded operation.

Fig. 20, the device is supplying zero real power to the microgrid while delivering the reactive power demand of 19kVAr to the microgrid such that unity power factor can be achieved at the grid side.

At $t = 0.16$ s, an isolation is initiated upon detection of a fault on the upstream network of the grid and CB 1 opens to disconnect the microgrid from the grid (see Fig. 1). It can be seen from Fig. 19 that the CB manages to fully isolate the microgrid from the grid in about half a cycle, resulting in zero real and reactive power delivered by the grid for $0.16 \leq t < 0.52$ s. With only the microgrid supplying for the loads, the power imbalance results in a decrease in the system frequency as shown in Fig. 21 for $0.16 \leq t < 0.36$ s. To maintain the stability of the microgrid during islanded operation, the proposed device is tasked to dispatch real power of 32 kW at $t = 0.36$ s by the microgrid energy management system while the reactive power of 19 kVAr to the microgrid is still maintained such that the total generation from the microgrid and the device can meet the load demand. A delay of 0.2 s is introduced between the islanding of the microgrid and the initiation of the device to cater for frequency transients in the system. As shown in Fig. 21, for $t \geq 0.36$ s, the frequency is gradually restored to its nominal value of 50 Hz. This test case demonstrates the capability of the device to supply all the real and reactive power to the microgrid when it is islanded from the grid.

VII. Conclusion

In this paper, a flexible ac distribution system device for microgrid applications has been presented. The proposed solution integrates EKF into the control design for frequency tracking and to extract the harmonic spectra of the grid voltage and the load currents. The device is installed at the PCC that the microgrid and other electrical networks are connected to and is designed to tackle a wide range of PQ issues. It also operates as a DG unit to perform load sharing when the cost of generation from the grid is high such that peak shaving is achieved and also during islanded operation of the microgrid. The design concept has been tested under several case scenarios and the results obtained verified that the device can handle a wide range of PQ issues, thus increasing the overall PQ and reliability of the microgrid. However, the proposed design concept still needs further validation by experimental studies because measurement errors due to inaccuracies of the voltage and current sensors, and modeling errors due to variations in system parameters could affect the performance of the device in practical implementation. The simulation results obtained in this paper and the current analysis serve as a fundamental step toward the design of control circuits for hardware implementation of the device in the future.

References

[1] R. Lasseter, J. Eto, B. Schenkman, J. Stevens, H. Vollkommer, D. Klapp, E. Linton, H. Hurtado, and J. Roy, "Certs microgrid laboratory test bed, and smart loads," *IEEE Trans. Power Del.*, vol. 26, no. 1, pp. 325–332, Jan. 2011.

[2] A. Chambers, S. Hamilton, and B. Schnoor, *Distributed Generation: A Nontechnical Guide*. Tulsa, OK, USA: PennWell, 2001.

[3] A. Luo, Z. Shuai, W. Zhu, and Z. J. Shen, "Combined system for harmonic suppression and reactive power compensation," *IEEE Trans. Ind. Electron.*, vol. 56, no. 2, pp. 418–428, Feb. 2009.

[4] L. H. Tey, P. L. So, and Y. C. Chu, "Improvement of power quality using adaptive shunt active filter," *IEEE Trans. Power Del.*, vol. 20, no. 2, pp. 1558–1568, Apr. 2005.

[5] A. Nasiri, Z. Nie, S. B. Bekiarov, and A. Emadi, "An on-line UPS system with power factor correction and electric isolation using BIFRED converter," *IEEE Trans. Ind. Electron.*, vol. 55, no. 2, pp. 722–730, Feb. 2008.

[6] M. Pascal, G. Garcerá, E. Figueres, and F. G. Espín, "Robust model-following control of parallel UPS single-phase inverters," *IEEE Trans. Ind. Electron.*, vol. 55, no. 8, pp. 2870–2883, Aug. 2008.

[7] A. Gosh, A. K. Jindal, and A. Joshi, "Design of a capacitor-supported dynamic voltage restorer (DVR) for unbalanced and distorted loads," *IEEE Trans. Power Del.*, vol. 19, no. 1, pp. 405–413, Jan. 2004.

[8] D. M. Vilathagamuwa, H. M. Wijekoon, and S. S. Choi, "A novel technique to compensate voltage sags in multiline distribution system–The interline dynamic voltage restorer," *IEEE Trans. Ind. Electron.*, vol. 54, no. 4, pp. 2249–2261, Aug. 2007.
[9] K. H. Kwan, Y. C. Chu, and P. L. So, "Model-based H∞ control of a unified power quality conditioner," *IEEE Trans. Ind. Electron.*, vol. 56, no. 7, pp. 2493–2502, Jul. 2009.
[10] A. Gosh and G. Ledwich, *Power Quality Enhancement Using Custom Power Devices*. Norwell, MA, USA: Kluwer, 2002, pp. 380–406.
[11] Y. C. Chu and M. Z. Q. Chen, "Efficient model predictive algorithms for tracking of periodic signals," *J. Control Sci. Eng.*, vol. 2012, pp. 1–13, 2012.
[12] A. Pigazo and V. M. Moreno, *Estimation of Electrical Power Quantities by Means of Kalman Filtering*. Vienna, Austria: InTech, 2009, pp. 375–396.
[13] J. Mattingley, Y. Wang, and S. Boyd, "Receding horizon control: Automatic generation of high-speed solvers," *IEEE Control Syst. Mag.*, vol. 31, no. 3, pp. 52–65, Jun. 2011.
[14] X. Liu, P. Wang, and P. C. Loh, "A hybrid AC/DC microgrid and its coordination control," *IEEE Trans. Smart Grid*, vol. 2, no. 2, pp. 278–286, Jun. 2011.
[15] C. Y. Teo, *Principles and Design of Low Voltage Systems*. Singapore: Byte Power Publications, 1997.

K. T. Tan (S'08) received the B.Eng. degree in electrical and electronic engineering from Nanyang Technological University, Nanyang, Singapore, in 2008, where he is currently working towards the Ph.D. degree in the Laboratory for Clean Energy Research, School of Electrical and Electronic Engineering.

His research interests include clean and renewable energy, microgrids, and smart grids.

P. L. So (M'98–SM'03) received the B.Eng. degree (with first class Hons.) in electrical engineering from the University of Warwick, Coventry, U.K., in 1993, and the Ph.D. degree in electrical power systems from Imperial College, University of London, London, U.K., in 1997.

He is currently an Associate Professor in the School of Electrical and Electronic Engineering, Nanyang Technological University, Nanyang, Singapore. Prior to his academic career, he worked for eleven years as a Second Engineer with China Light and Power Company Limited, Hong Kong, in the field of power system protection. His research interests include power system stability and control, power quality, power line communications, clean and renewable energy, energy management, microgrids, and smart grids.

Dr. So was the Chair of the IEEE Singapore Section from 2009 to 2010. He is currently a member of the Electrical Testing Technical Committee, Singapore Accreditation Council, and a Member of Working Group under the purview of the Telecommunications Standards Technical Committee, Infocomm Development Authority (iDA) of Singapore.

Y. C. Chu (S'88–M'97–SM'06) received the B.Sc. degree in electronics and the M.Phil. degree in information engineering from the Chinese University of Hong Kong, Hong Kong, in 1990 and 1992, respectively, and the Ph.D. degree in Control from the University of Cambridge, Cambridge, U.K., in 1996.

He was a Postdoctoral Fellow with the Chinese University of Hong Kong, a Research Associate with the University of Cambridge, an Assistant Professor and subsequently an Associate Professor with the Nanyang Technological University, Singapore. From 2011 to 2012, he was a Visiting Associate Professor with the University of Hong Kong, Hong Kong. His research interests include control theory and artificial neural networks, with applications to spacecraft, underwater vehicles, combustion oscillations, microgrids, and smart grids.

Dr. Chu was a Croucher Scholar in 1993–1995 and has been a Fellow of the Cambridge Philosophical Society since 1993.

M. Z. Q. Chen (M'08) received the B.Eng. degree in electrical and electronic engineering from Nanyang Technological University, Nanyang, Singapore, in 2003, and the Ph.D. degree in control engineering from Cambridge University, Cambridge, U.K., in 2007.

He is currently an Assistant Professor in the Department of Mechanical Engineering, the University of Hong Kong, Hong Kong.

Dr. Chen is a Fellow of the Cambridge Philosophical Society and a Life Fellow of the Cambridge Overseas Trust. Since 2008, he has been a Reviewer of the IEEE TRANSACTIONS ON AUTOMATIC CONTROL, *Automatica*, *International Journal of Robust and Nonlinear Control, International Journal of Adaptive Control and Signal Processing, International Journal of Systems Science, and Journal of Sound and Vibration*, amongst others. He is currently a Guest Associate Editor for the *International Journal of Bifurcation and Chaos.*